CHALMERS
UNIVERSITY OF TECHNOLOGY

Macroscale modelling of 3D-woven composites: Elasto-plasticity and progressive damage

Citation for the original published paper (version of record):
Oddy, C., Ekh, M., Fagerström, M. (2022). Macroscale modelling of 3D-woven composites: Elasto-plasticity and progressive damage. International Journal of Solids and Structures, 250. http://dx.doi.org/10.1016/j.ijsolstr.2022.111696

International Journal of Solids and Structures 250 (2022) 111696

Contents lists available at ScienceDirect

International Journal of Solids and Structures

journal homepage: www.elsevier.com/locate/ijsolstr

Macroscale modelling of 3D-woven composites: Elasto-plasticity and progressive damage

Carolyn Oddy *, Magnus Ekh, Martin Fagerström

Department of Industrial and Materials Science, Chalmers University of Technology, SE-412 96 Gothenburg, Sweden

ARTICLE INFO

Keywords:
3D-woven composite
Elasto-plasticity
Damage
Macroscale modelling
Finite element modelling

ABSTRACT

There is a growing need across multiple industries for lightweight materials with improved material performance and reduced manufacturing costs. Composites with 3D-woven reinforcement could help fill this need. Their use however, requires the development of computationally efficient and industrially applicable material models to predict their non-linear behaviour. This work proposes a macroscale elasto-plasticity and damage model to capture the experimentally observed inelastic strains and stiffness reductions. The model is general, thermodynamically consistent and allows for various non-linear phenomena to be added and calibrated in a modular fashion depending on loading direction. Further it allows for a simplified parameter identification routine in which the damage and hardening laws are identified directly from experimental curves without the need for complex calibration routines.

In order to demonstrate the applicability of the proposed macroscale model, focus is given to predicting the material response of a 3D glass fibre reinforced epoxy material system. The damage and hardening parameters are identified based on uniaxial tensile and in-plane shear experimental curves with unloading cycles. The model performance is validated against an off-axis tensile test with unloading cycles and shows good agreement to the experimental result.

1. Introduction

Composites with 3D-woven reinforcements have a broad list of reported benefits. The through thickness reinforcements in particular, as discussed by Bogdanovich (2007), create a material which can outperform laminated composites in many aspects. Composites with 3D-woven reinforcement are able to suppress delamination and provide high out-of-plane strength and stiffness, as well as fracture toughness and damage tolerance. Further, both Khokar et al. (2015) and Kazemahvazi et al. (2016) have shown that 3D-woven composites have promising specific energy absorption capabilities. With all of their advantages, composites with 3D-woven reinforcement are starting to appear in industrial applications. This includes in the landing gear braces of the Boeing 787 (Nathan, 2015) as well as in aero-engines (De Luycker et al., 2009). However, to drive their use in further applications, efficient modelling techniques are needed that can predict how 3D-woven composites deform and eventually fail.

Capturing the deformation and failure of 3D-woven composites, requires the consideration of a number of competing mechanisms. As shown in Fig. 1(a), this includes linear elasticity in region I, followed by region II with progressive damage and inelasticity and finally, failure and softening in region III. Current modelling approaches found in the literature primarily focus on capturing these behaviours on the mesoscale using finite element (FE) models. These FE models require the creation of a mesoscale representative volume element (RVE). Here the yarns are modelled as homogeneous anisotropic bodies surrounded by an isotropic matrix. Creating this RVE in itself can be a challenging task, as discussed by Stig and Hallström (2012b) as well as Lomov et al. (2007). Once the RVE is generated, viscoelastic material behaviour has been added to the matrix and yarns by for example (Hirsekorn et al., 2018). Others such as Lomov et al. (2009) and Green et al. (2014) have turned to continuum damage mechanics to progressively degrade the stiffness of the matrix and yarns through pertinent damage evolution laws.

While explicitly modelling the reinforcement architecture allows for a detailed understanding and prediction of the mesoscale response, it is also computationally expensive. Modelling large structural components in this way is therefore infeasible. An appealing alternative is to adopt a (largely) macroscopic modelling approach. An interesting example has been proposed by El Said et al. (2018), where only the critically loaded regions are modelled on the mesoscale. The remaining domain is then considered as a homogeneous anisotropic solid. Alternatively, other authors have proposed to model the entire domain on the macroscale.

* Corresponding author.
E-mail address: carolyn.oddy@chalmers.se (C. Oddy).

https://doi.org/10.1016/j.ijsolstr.2022.111696
Received 8 October 2021; Received in revised form 4 April 2022; Accepted 3 May 2022
Available online 14 May 2022

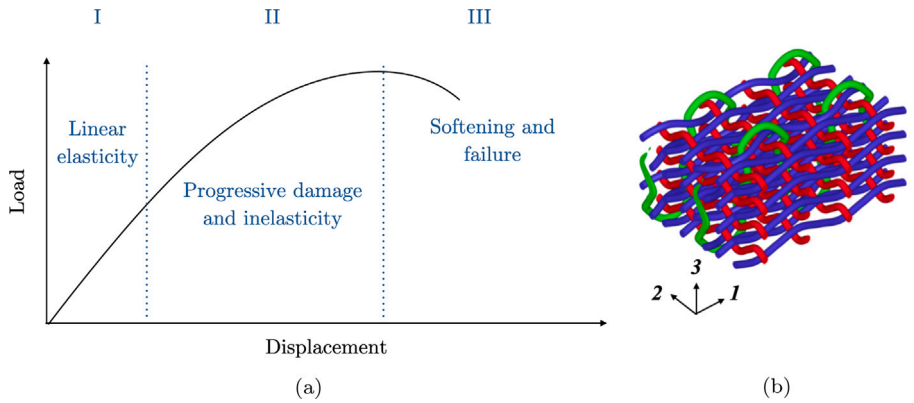

Fig. 1. (a) Components of a macroscale model for 3D-woven composites. (b) schematic of 3D-woven preform. Blue yarns are warp, red and green yarns are horizontal and vertical weft respectively.

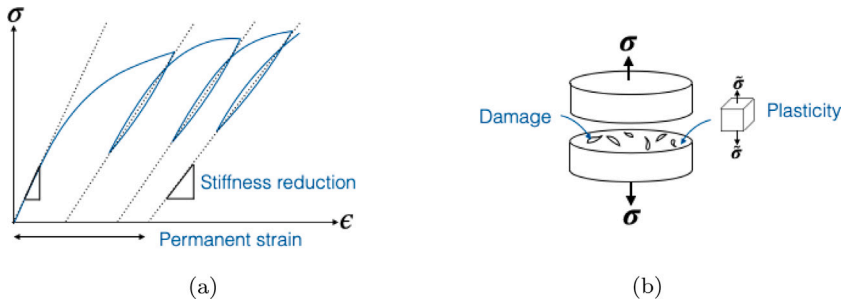

Fig. 2. Illustration of the model assumptions. (a) Schematic showing stiffness reduction and permanent strain development. (b) Schematic illustrating the stress and effective stress.

One example of a macroscale model is the ONERA Damage Model for Polymer Matrix Composites, which is able to capture a variety of experimentally observed phenomena such as anisotropic damage growth and viscous behaviours, cf. Marcin (2010) and Hurmane et al. (2016). As discussed by Marcin (2010), macroscale models in particular show the most industrial relevance.

This work therefore takes steps towards proposing a macroscale phenomenological model to capture region II in Fig. 1(a), using plasticity and continuum damage mechanics. In particular, focus is given to formulating a model that provides a clear and simple calibration routine that directly links parameters to experimental tests. The considered weave architecture, shown in Fig. 1(b), creates a material which is highly anisotropic in nature. The interlacement of warp (blue), horizontal weft (red) and vertical weft (green) yarns, means that the development of both the damage and plasticity are strongly dependent on loading direction. In order to address the challenges associated with macroscale modelling of such an anisotropic material, two main themes are discussed in this paper.

Firstly, a modelling framework previously proposed by Oddy et al. (2021) is introduced. This framework allows for the addition of four scalar damage variables and plastic phenomena in a modular fashion depending on loading direction (i.e. in shear or along each reinforcement direction). Secondly, it is then necessary to determine how these damage variables and plastic phenomena should develop in tandem with one another in each loading direction.

In the case of Lemaitre (1992) for example, the plastic deformation is kinetically coupled to the damage. In the current work however, a number of simplifying assumptions are made, that better reflect what is considered by Ladeveze and LeDantec (1992) and Zscheyge et al. (2020). These assumptions are, as illustrated in Fig. 2(a), that damage strictly leads to a reduction in the material stiffness. Plasticity on the other hand is assumed to lead to the development of permanent strain. Further, as illustrated in Fig. 2(b) it is assumed that while the damaged material is subjected to a stress $\boldsymbol{\sigma}$, plasticity solely acts on the undamaged material which is subjected to a higher effective stress, $\tilde{\boldsymbol{\sigma}}$. These assumptions decouple the development of damage and inelastic strains. This in turn, simplifies parameter identification, and allow for damage and plasticity laws to be identified directly from the uniaxial cyclic stress–strain curves without the need for complex calibration schemes. It also simplifies the implementation procedure.

The proposed model framework and parameter identification routine is applied to the case of a 3D-woven glass fibre reinforced epoxy. Experimental results from cyclic tensile testing along the reinforcement directions as well as in plane shear testing are used to calibrate the damage and plasticity development. Specific attention is given to discussing the challenges associated with capturing the shear behaviour of 3D-woven composites. The model is then validated against an off-axis tensile test and provides good agreement to the experimental results. This model is thermodynamically consistent, flexible and provides a clear calibration routine that links parameters directly to experimental results.

2. A modelling framework for 3D-woven composites

The architecture of the fibre reinforcements of 3D-woven composites creates a material that can be highly anisotropic by nature. Further, a number of factors can lead to varying levels of anisotropy. This can include everything from the classification of the 3D-weave type (i.e. layer-to-layer interlock, angle interlock, orthogonal) to how balanced the weave is in each reinforcement direction. Determining all terms in the stiffness tensor, in particular for complex couplings between in-plane or out-of-plane tensile or shear behaviours, is not a trivial task experimentally. The use of mesoscale RVEs can, in some cases be used to gain a deeper understanding in these complex couplings.

This work primarily focuses on the use of orthogonal 3D-woven composites, in which there are three mutually perpendicular reinforcement directions. When analysing their mesoscale volume element of a plain orthogonal 3D weave, Stig and Hallström (2012a) demonstrated

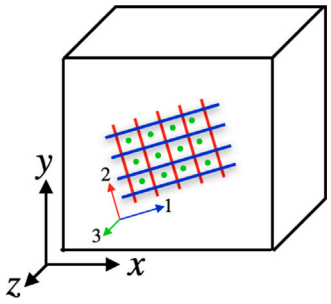

Fig. 3. Illustration of the local and global coordinate systems.

that it was in fact orthotropic. For these reasons, the starting point for the model presented in this work is the assumption of elastic orthotropy. More specifically, the 3D-woven composite is described by 3 principal directions, defined by the nominal yarn directions, each holding distinct material properties.

A modelling framework based on the assumption of orthotropy by Oddy et al. (2021) is therefore proposed. The framework is summarised in the following section after a brief introduction to structural tensors and elastic orthotropy. Four scalar damage variables and their associated onset surfaces are then introduced. This is followed by the introduction of four plastic yield surfaces, their related hardening laws and flow rules. Finally, the thermodynamic aspects of the model are discussed.

2.1. Structural tensors and elastic orthotropy

In the local 123-system shown in Fig. 3, the stiffness of the orthotropic 3D-woven composite can be expressed in Voigt form using 9 elastic engineering parameters. Specifically these are Young's moduli (E_1, E_2, E_3), shear moduli (G_{12}, G_{23}, G_{13}) and Poisson's ratios (ν_{12}, ν_{23}, ν_{13}). Then in the local coordinate system, the Voigt stiffness matrix can be written as

$$\underline{\mathbb{E}} = \begin{bmatrix} \frac{E_1(1-\nu_{32}\nu_{23})}{\Delta} & \frac{E_1(\nu_{21}+\nu_{31}\nu_{23})}{\Delta} & \frac{E_1(\nu_{31}+\nu_{21}\nu_{32})}{\Delta} & 0 & 0 & 0 \\ \frac{E_2(\nu_{12}+\nu_{13}\nu_{32})}{\Delta} & \frac{E_2(1-\nu_{31}\nu_{13})}{\Delta} & \frac{E_2(\nu_{32}+\nu_{31}\nu_{12})}{\Delta} & 0 & 0 & 0 \\ \frac{E_3(\nu_{13}+\nu_{12}\nu_{23})}{\Delta} & \frac{E_3(\nu_{23}+\nu_{13}\nu_{21})}{\Delta} & \frac{E_3(1-\nu_{12}\nu_{21})}{\Delta} & 0 & 0 & 0 \\ 0 & 0 & 0 & G_{12} & 0 & 0 \\ 0 & 0 & 0 & 0 & G_{23} & 0 \\ 0 & 0 & 0 & 0 & 0 & G_{13} \end{bmatrix} \tag{1}$$

where

$$\Delta = 1 - \nu_{12}\nu_{21} - \nu_{23}\nu_{32} - \nu_{31}\nu_{13} - 2\nu_{12}\nu_{23}\nu_{31}. \tag{2}$$

As the local reinforcement orientation generally varies over a component, using this stiffness representation would require a method for point-wise coordinate transformations.

An alternative representation of the stiffness can be made through the use of structural tensors. In this way the global stiffness tensor $\mathbb{E}$ is described based on the reinforcement orientation at each material point. This reinforcement orientation is given by three vectors $\boldsymbol{a}^1$, $\boldsymbol{a}^2$ and $\boldsymbol{a}^3$, which describe the nominal direction of the warp, horizontal weft and vertical weft yarns respectively. It is then possible to formulate three second order structural tensors

$$\boldsymbol{A}^I = \boldsymbol{a}^I \otimes \boldsymbol{a}^I, \text{ for } I = 1,2,3 \tag{3}$$

and three fourth order tensor $\mathbb{A}^I$, where[1]

$$\mathbb{A}^I = \frac{1}{2}\left(\boldsymbol{A}^I \bar{\otimes} \boldsymbol{I} + \boldsymbol{I} \bar{\otimes} \boldsymbol{A}^I\right), \text{ for } I = 1,2,3. \tag{4}$$

[1] The non-standard $\bar{\otimes}$ operator expresses the operation $\left(\boldsymbol{A}\bar{\otimes}\boldsymbol{B}\right)_{ijkl} = A_{ik}B_{jl}$.

Here $\boldsymbol{I}$ denotes the second order identity tensor. From the introduction of $\boldsymbol{A}^I$ and $\mathbb{A}^I$, the global elastic stiffness tensor $\mathbb{E}$, can be expressed as

$$\mathbb{E} = \sum_{I=1}^{3} \varphi_I \mathbb{A}^I + \sum_{I=1}^{3}\sum_{J=1}^{3} \phi_{IJ} \boldsymbol{A}^I \otimes \boldsymbol{A}^J. \tag{5}$$

Again, 9 constants are required to describe the elastic behaviour of the material, φ_I and $\phi_{IJ} = \phi_{JI}$. They can be found by considering the case when the local and global coordinate systems are aligned. Specifically when $\boldsymbol{a}^1 = \begin{bmatrix}1 & 0 & 0\end{bmatrix}^T$, $\boldsymbol{a}^2 = \begin{bmatrix}0 & 1 & 0\end{bmatrix}^T$ and $\boldsymbol{a}^3 = \begin{bmatrix}0 & 0 & 1\end{bmatrix}^T$. Then in Voigt form, Eq. (5) becomes

$$\underline{\mathbb{E}} = \begin{bmatrix} \phi_{11}+\varphi_1 & \phi_{12} & \phi_{13} & 0 & 0 & 0 \\ \phi_{12} & \phi_{22}+\varphi_2 & \phi_{23} & 0 & 0 & 0 \\ \phi_{13} & \phi_{23} & \phi_{33}+\varphi_3 & 0 & 0 & 0 \\ 0 & 0 & 0 & 1/4(\varphi_1+\varphi_2) & 0 & 0 \\ 0 & 0 & 0 & 0 & 1/4(\varphi_2+\varphi_3) & 0 \\ 0 & 0 & 0 & 0 & 0 & 1/4(\varphi_3+\varphi_1) \end{bmatrix}. \tag{6}$$

As a consequence the elastic constants can be found by directly by comparing Eqs. (1) to (6).

2.2. A structural tensor based constitutive framework

The proposed general framework for modelling 3D-woven composites is based on the work of Spencer (1984) for fibre-reinforced composites. It involves decomposing the stress tensor into four different terms: one containing the shear stress components $\boldsymbol{s}$, the others containing the components along the reinforcement directions. That is that,

$$\boldsymbol{\sigma} = \boldsymbol{s} + \sum_{I=1}^{3} (\boldsymbol{\sigma} : \boldsymbol{A}^I)\boldsymbol{A}^I = \boldsymbol{s} + \sum_{I=1}^{3} T^I \boldsymbol{A}^I. \tag{7}$$

The scalar measure T^I has been introduced here. In this sense, T^I represents the magnitude of the stress in each reinforcement direction.

To help visualise this, consider again the case where the local and global coordinate systems align. Eq. (7) can then be expressed in matrix form as

$$\boldsymbol{\sigma} = \underbrace{\begin{bmatrix} 0 & \sigma_{12} & \sigma_{13} \\ \sigma_{12} & 0 & \sigma_{23} \\ \sigma_{13} & \sigma_{23} & 0 \end{bmatrix}}_{\boldsymbol{s}} + \underbrace{\begin{bmatrix} \sigma_{11} & 0 & 0 \\ 0 & 0 & 0 \\ 0 & 0 & 0 \end{bmatrix}}_{(\boldsymbol{\sigma}:\boldsymbol{A}^1)\boldsymbol{A}^1} + \underbrace{\begin{bmatrix} 0 & 0 & 0 \\ 0 & \sigma_{22} & 0 \\ 0 & 0 & 0 \end{bmatrix}}_{(\boldsymbol{\sigma}:\boldsymbol{A}^2)\boldsymbol{A}^2} + \underbrace{\begin{bmatrix} 0 & 0 & 0 \\ 0 & 0 & 0 \\ 0 & 0 & \sigma_{33} \end{bmatrix}}_{(\boldsymbol{\sigma}:\boldsymbol{A}^3)\boldsymbol{A}^3}. \tag{8}$$

By decomposing the strain tensor in the same way, i.e. as

$$\boldsymbol{\epsilon} = \boldsymbol{e} + \sum_{I=1}^{3} (\boldsymbol{\epsilon} : \boldsymbol{A}^I)\boldsymbol{A}^I, \tag{9}$$

it is also possible to divide it into separate terms containing the shear strain components, $\boldsymbol{e}$, and the components oriented in the reinforcement direction, $(\boldsymbol{\epsilon} : \boldsymbol{A}^I)\boldsymbol{A}^I$.

At this point, a fourth order tensor $\mathbb{Q}$ can be introduced. This tensor allows for a convenient way to relate $\boldsymbol{s}$ and $\boldsymbol{\sigma}$ as well as $\mathbf{e}$ and $\boldsymbol{\epsilon}$. More specifically,

$$\boldsymbol{s} = \mathbb{Q} : \boldsymbol{\sigma}, \quad \text{and } \boldsymbol{e} = \mathbb{Q} : \boldsymbol{\epsilon}, \tag{10}$$

where

$$\mathbb{Q} = \mathbb{I} - \sum_{I=1}^{3} \boldsymbol{A}^I \otimes \boldsymbol{A}^I \tag{11}$$

and $\mathbb{I}$ is the fourth order identity tensor.

Combining the equations for stress and strain in Eqs. (7) and (9) with the expression for elastic orthotropy in Eq. (5) gives the final constitutive framework. Again it has four terms holding the components

in shear, and along the reinforcement directions. Then, still considering pure elasticity, one obtains

$$\boldsymbol{\sigma} = \underbrace{\mathbb{E}_m : \boldsymbol{e}}_{\text{shear}} + \underbrace{\mathbb{E}_{f1} : \boldsymbol{\epsilon}}_{\text{warp}} + \underbrace{\mathbb{E}_{f2} : \boldsymbol{\epsilon}}_{\text{h. weft}} + \underbrace{\mathbb{E}_{f3} : \boldsymbol{\epsilon}}_{\text{v. weft}} \tag{12}$$

where

$$\mathbb{E}_m = \sum_{I=1}^{3} \varphi_I \mathbb{A}^I, \text{ and } \mathbb{E}_{fI} = \varphi_I \boldsymbol{A}^I \otimes \boldsymbol{A}^I + \frac{1}{2}\sum_{J=1}^{3} \phi_{IJ}\left(\boldsymbol{A}^I \otimes \boldsymbol{A}^J + \boldsymbol{A}^J \otimes \boldsymbol{A}^I\right). \tag{13}$$

In Voigt form, again when $\boldsymbol{a}^1 = \begin{bmatrix}1 & 0 & 0\end{bmatrix}^T$, $\boldsymbol{a}^2 = \begin{bmatrix}0 & 1 & 0\end{bmatrix}^T$ and $\boldsymbol{a}^3 = \begin{bmatrix}0 & 0 & 1\end{bmatrix}^T$, Eq. (12) is given by

$$\begin{bmatrix}\sigma_{11}\\ \sigma_{22}\\ \sigma_{33}\\ \sigma_{12}\\ \sigma_{23}\\ \sigma_{13}\end{bmatrix} = \begin{bmatrix}\varphi_1 & 0 & 0 & 0 & 0 & 0\\ 0 & \varphi_2 & 0 & 0 & 0 & 0\\ 0 & 0 & \varphi_3 & 0 & 0 & 0\\ 0 & 0 & 0 & \frac{\varphi_1+\varphi_2}{4} & 0 & 0\\ 0 & 0 & 0 & 0 & \frac{\varphi_2+\varphi_3}{4} & 0\\ 0 & 0 & 0 & 0 & 0 & \frac{\varphi_1+\varphi_3}{4}\end{bmatrix}\begin{bmatrix}0\\0\\0\\ \gamma_{12}\\ \gamma_{23}\\ \gamma_{13}\end{bmatrix} + \begin{bmatrix}\phi_{11}+\varphi_1 & \frac{\phi_{12}}{2} & \frac{\phi_{13}}{2} & 0 & 0 & 0\\ \frac{\phi_{12}}{2} & 0 & 0 & 0 & 0 & 0\\ \frac{\phi_{13}}{2} & 0 & 0 & 0 & 0 & 0\\ 0 & 0 & 0 & 0 & 0 & 0\\ 0 & 0 & 0 & 0 & 0 & 0\\ 0 & 0 & 0 & 0 & 0 & 0\end{bmatrix}\begin{bmatrix}\epsilon_{11}\\ \epsilon_{22}\\ \epsilon_{33}\\ \gamma_{12}\\ \gamma_{23}\\ \gamma_{13}\end{bmatrix} + \begin{bmatrix}0 & \frac{\phi_{12}}{2} & 0 & 0 & 0 & 0\\ \frac{\phi_{12}}{2} & \phi_{22}+\varphi_2 & \frac{\phi_{23}}{2} & 0 & 0 & 0\\ 0 & \frac{\phi_{23}}{2} & 0 & 0 & 0 & 0\\ 0 & 0 & 0 & 0 & 0 & 0\\ 0 & 0 & 0 & 0 & 0 & 0\\ 0 & 0 & 0 & 0 & 0 & 0\end{bmatrix}\begin{bmatrix}\epsilon_{11}\\ \epsilon_{22}\\ \epsilon_{33}\\ \gamma_{12}\\ \gamma_{23}\\ \gamma_{13}\end{bmatrix} + \begin{bmatrix}0 & 0 & \frac{\phi_{13}}{2} & 0 & 0 & 0\\ 0 & 0 & \frac{\phi_{23}}{2} & 0 & 0 & 0\\ \frac{\phi_{13}}{2} & \frac{\phi_{23}}{2} & \phi_{33}+\varphi_3 & 0 & 0 & 0\\ 0 & 0 & 0 & 0 & 0 & 0\\ 0 & 0 & 0 & 0 & 0 & 0\\ 0 & 0 & 0 & 0 & 0 & 0\end{bmatrix}\begin{bmatrix}\epsilon_{11}\\ \epsilon_{22}\\ \epsilon_{33}\\ \gamma_{12}\\ \gamma_{23}\\ \gamma_{13}\end{bmatrix}.$$

As previously discussed, this framework allows inelastic phenomena to be introduced modularly based on the loading direction. It is therefore possible to define one scalar damage variable in shear d_s and one damage variable associated to each reinforcement direction d_1, d_2 and d_3. Further, by splitting the strain additively into elastic and plastic parts, i.e. where

$$\boldsymbol{\epsilon} = \boldsymbol{\epsilon}_{el} + \boldsymbol{\epsilon}_p$$

it is possible to formulate the constitutive relationship describing the stress as

$$\boldsymbol{\sigma} = (1-d_s)\mathbb{E}_m : (\boldsymbol{e} - \boldsymbol{e}_p) + \sum_{I=1}^{3}(1-d_I)\mathbb{E}_{fI} : (\boldsymbol{\epsilon} - \boldsymbol{\epsilon}_p). \tag{14}$$

Note that, the corresponding effective stress $\tilde{\boldsymbol{\sigma}}$ is given by

$$\tilde{\boldsymbol{\sigma}} = \mathbb{E}_m : \boldsymbol{e}_{el} + \left(\mathbb{E}_{f1} + \mathbb{E}_{f2} + \mathbb{E}_{f3}\right) : \boldsymbol{\epsilon}_{el} \tag{15}$$

which is essentially Eq. (12) with the strain replaced by the elastic strain.

2.2.1. Damage

The method for determining the evolution for each damage variable is discussed in greater detail in Section 3. So far, we note that each damage variable must then also be associated to a damage onset surface. In general terms, the damage onset surface in shear, denoted $\phi_{d,s}$, can be constructed from the damage driving force in shear Y_s and a measure η_s which controls the growth and evolution of the damage surface. Then,

$$\phi_{d,s} = Y_s - \eta_s(d_s) \leq 0. \tag{16}$$

Similarly, damage onset surfaces in each reinforcement direction $\phi_{d,I}$, can be introduced where

$$\phi_{d,I} = Y_I - \eta_I(d_I) \leq 0, \text{ for } I = 1,2,3. \tag{17}$$

Again, Y_I denotes the damage driving force in each reinforcement direction and η_I the associated function controlling the damage evolution. The associated damage growth conditions are then

$$\dot{d}_s \geq 0, \quad \phi_{d,s} \leq 0, \quad \dot{d}_s\phi_{d,s} = 0,$$

and

$$\dot{d}_I \geq 0, \quad \phi_{d,I} \leq 0, \quad \dot{d}_I\phi_{d,I} = 0, \quad \text{for } I = 1,2,3.$$

The explicit expressions for the damage driving forces are discussed in greater detail in Section 2.3. At this stage, we note that they are defined by differentiating the free energy Ψ with respect to the damage variables, i.e.

$$Y_s = -\frac{\partial \Psi}{\partial d_s} = \frac{1}{2}\boldsymbol{e}_{el} : \mathbb{E}_m : \boldsymbol{e}_{el} \tag{18}$$

and

$$Y_I = -\frac{\partial \Psi}{\partial d_I} = \frac{1}{2}\boldsymbol{\epsilon}_{el} : \mathbb{E}_{f,I} : \boldsymbol{\epsilon}_{el} \tag{19}$$

respectively. The selection of η_s and η_I are based on experimental results, see Section 3.

The associated loading conditions are then

$$\dot{d}_s \geq 0, \quad \phi_{d,s} \leq 0, \quad \dot{d}_s\phi_{d,s} = 0$$

and

$$\dot{d}_I \geq 0, \quad \phi_{d,I} \leq 0, \quad \dot{d}_I\phi_{d,I} = 0, \quad \text{for } I = 1,2,3.$$

2.2.2. Plasticity

When it comes to the development of plastic strains, four yield surfaces based on the (undamaged) effective stresses are needed: one in shear, $\phi_{p,s}$ and one for each reinforcement direction $\phi_{p,I}$ for $I = 1,2,3$. The experimental results presented in Section 5, remain in the positive stress–strain quadrant. The hardening is therefore restricted to be of isotropic type.

In shear, defining the yield surface requires prescribing a yield stress in shear $\tau_{y,s}$ and an expression for the isotropic hardening stress κ_s as a function of an internal hardening variable k_s. Then

$$\phi_{p,s} = \frac{1}{\sqrt{2}}|\tilde{\boldsymbol{s}}| - \tau_y - \kappa_s(k_s) \leq 0, \tag{20}$$

where $\tilde{\boldsymbol{s}}$ denotes the effective shear stress tensor and $|\tilde{\boldsymbol{s}}| = \sqrt{\tilde{\boldsymbol{s}} : \tilde{\boldsymbol{s}}}$.

Similarly the yield surface along each reinforcement direction can be defined as

$$\phi_{p,I} = |\tilde{T}^I| - \sigma_{y,I} - \kappa_I(k_I) \leq 0, \text{ for } I = 1,2,3, \tag{21}$$

where κ_I represents the isotropic hardening stress and $\sigma_{y,I}$ the yield stress associated with each reinforcement direction. The method for proposing appropriate expressions for the isotropic hardening stresses κ_s and κ_I, is discussed in greater detail in Section 3.

The development of plastic strain can be defined using a non-associative flow rule (i.e. where the differentiation of the yield surface takes place using the effective stress instead of the stress, which is discussed in 2.3), where in shear

$$\dot{\boldsymbol{e}}_p = \dot{\lambda}_s\frac{\partial \phi_{p,s}}{\partial \tilde{\boldsymbol{\sigma}}} = \dot{\lambda}_s\frac{\partial \phi_{p,s}}{\partial \tilde{\boldsymbol{s}}} = \dot{\lambda}_s\frac{\tilde{\boldsymbol{s}}}{\sqrt{2}|\tilde{\boldsymbol{s}}|}, \tag{22}$$

and along the reinforcement directions

$$\dot{\epsilon}_{p,I} = \dot{\lambda}_I \frac{\partial \phi_{p,I}}{\partial \tilde{\sigma}} = \dot{\lambda}_I \text{sgn}\left(\tilde{\sigma} : \boldsymbol{A}^I\right) \boldsymbol{A}^I, \text{ for } I = 1,2,3. \tag{23}$$

The total plastic strain is then

$$\epsilon_p = e_p + \sum_{I=1}^{3} \epsilon_{p,I}. \tag{24}$$

Note that since $\boldsymbol{A}^I : \boldsymbol{A}^J = 0$ and $\boldsymbol{A}^I : e = 0$ the plastic strain development $\dot{\epsilon}_{p,I}$ will (by construction) only influence the term related to its reinforcement direction.

Similarly, the evolution of internal hardening variables in shear and along the reinforcement directions can be expressed as

$$\dot{k}_s = \dot{\lambda}_s \frac{\partial \phi_{p,s}}{\partial \kappa_s} = -\dot{\lambda}_s \tag{25}$$

and

$$\dot{k}_I = \dot{\lambda}_I \frac{\partial \phi_{p,I}}{\partial \kappa^I} = -\dot{\lambda}_I, \text{ for } I = 1,2,3 \tag{26}$$

respectively. Finally, the conditions on plastic strain development are given by

$$\dot{\lambda}_s \geq 0, \quad \phi_{p,s} \leq 0, \quad \dot{\lambda}_s \phi_{p,s} = 0 \tag{27}$$

$$\dot{\lambda}_I \geq 0, \quad \phi_{p,I} \leq 0, \quad \dot{\lambda}_I \phi_{p,I} = 0, \text{ for } I = 1,2,3. \tag{28}$$

2.3. Thermodynamic considerations

The starting point of the thermodynamic formulation is that the dissipation inequality must satisfy

$$\sigma : \dot{\epsilon} - \dot{\Psi} \geq 0. \tag{29}$$

Given the additive decomposition of the strain tensor into the elastic and plastic parts, i.e.

$$\epsilon = \epsilon_{el} + \epsilon_p, \tag{30}$$

and the assumption that the free energy Ψ is a function of ϵ_{el}, d_s, d_I, k_s and k_I for $I = 1,2,3$, the two terms in the dissipation inequality can be expressed as

$$\sigma : \dot{\epsilon} = \sigma : \dot{\epsilon}_{el} + \sigma : \dot{\epsilon}_p \tag{31}$$

and

$$\dot{\Psi} = \frac{\partial \Psi}{\partial \epsilon_{el}} : \dot{\epsilon}_{el} + \frac{\partial \Psi}{\partial d_s}\dot{d}_s + \sum_{I=1}^{3} \frac{\partial \Psi}{\partial d_I}\dot{d}_I + \frac{\partial \Psi}{\partial k_s}\dot{k}_s + \sum_{I=1}^{3} \frac{\partial \Psi}{\partial k_I}\dot{k}_I, \tag{32}$$

respectively.

Combining Eqs. (31) and (32) and assuming with standard argumentation that $\sigma = \partial \Psi / \partial \epsilon_{el}$, leads to the reduced dissipation inequality

$$D = \sigma : \dot{\epsilon}_p - \frac{\partial \Psi}{\partial d_s}\dot{d}_s - \sum_{I=1}^{3} \frac{\partial \Psi}{\partial d_I}\dot{d}_I - \frac{\partial \Psi}{\partial k_s}\dot{k}_s - \sum_{I=1}^{3} \frac{\partial \Psi}{\partial k_I}\dot{k}_I \geq 0. \tag{33}$$

From this is it possible to identify the damage driving forces and isotropic hardening stresses as

$$Y_s = -\frac{\partial \Psi}{\partial d_s}, \quad Y_I = -\frac{\partial \Psi}{\partial d_I}, \quad \kappa_s = -\frac{\partial \Psi}{\partial k_s}, \quad \kappa_I = -\frac{\partial \Psi}{\partial k_I} \quad \text{for } I = 1,\ 2,\ 3. \tag{34}$$

Note here, that the stress σ is energy conjugated to the plastic strain development. Using an associative flow rule to define the plastic strain development, would require that the yield surfaces are differentiated with respect to σ. As previously discussed however, in order to ease the parameter identification and implementation process non-associative flow rules are chosen. Specifically, the yield surfaces are differentiated with respect to the effective stress $\tilde{\sigma}$, cf. Eqs. (22) and (23).

With a specific choice of free energy, it becomes possible to define more explicit expressions for the stress, damage driving forces and isotropic hardening stresses. In more detail, the free energy is assumed to be given by an elastic component and a plastic component. The plastic component, denoted here as Ψ_p can be determined based on the primitive functions of a chosen hardening law. Remaining generic here in terms of the plastic behaviour, the free energy can be expressed as

$$\Psi = \frac{1}{2}\left(1 - d_s\right) e_{el} : \mathbb{E}_m : e_{el} + \sum_{I=1}^{3} \frac{1}{2}\left(1 - d_I\right) \epsilon_{el} : \mathbb{E}_{fI} : \epsilon_{el} + \Psi_p(k_s, k_I).$$

As previously presented in Section 2.2.1, the thermodynamic driving forces for the damage variables become

$$Y_s = -\frac{\partial \Psi}{\partial d_s} = \frac{1}{2} e_{el} : \mathbb{E}_m : e_{el} \quad \text{and}$$

$$Y_I = -\frac{\partial \Psi}{\partial d_I} = \frac{1}{2} \epsilon_{el} : \mathbb{E}_{fI} : \epsilon_{el} \quad \text{for } I = 1,\ 2,\ 3.$$

Similarly, depending on the choice of hardening model, the isotropic hardening stresses are expressed as

$$\kappa_s = -\frac{\partial \Psi_p}{\partial k_s} \quad \text{and } \kappa_I = -\frac{\partial \Psi_p}{\partial k_s} \quad \text{for } I = 1,\ 2,\ 3.$$

3. Parameter identification scheme for damage and plasticity

Under pure shear or uniaxial loading along the reinforcements, the 3D constitutive stress–strain relationship in Eq. (14) is assumed to reduce to a scalar stress–strain relationship. While, due to the symmetric nature of the stiffness tensor, this is not truly the case, the degree of error caused by this simplification is (for most practical cases) minimal. A more in-depth discussion can be found in Appendix.

By using a 1D constitutive relationship for the purpose of calibration, the evolution of the damage and plasticity variables can be identified for each loading direction independently for each test. Damage can be quantified by considering the material stiffness reduction at each unloading cycle. Plasticity on the other hand can be assessed by tracking how strains persist at each unloading cycle. The proposed parameter identification routine is illustrated in Fig. 4. The outlined procedure is described generically for all load cases including shear. In the case of shear loading however, the shear modulus is determined instead of the Young's modulus. Note that here the subscripts denote the unloading cycle number. In more details, the illustrated procedure is:

1. Determine the onset of plasticity and damage, which can be at different points along the stress–strain curve. The choice of onset locations can be chosen depending on where non-linearity begins to appear in the curve and on the data that is available. For example, acoustic emissions or accelerometer outputs can be used to indicate the onset of damage. Unloading cycles carried out early enough in the test that show either no loss in stiffness or no development of permanent strain can also help indicate plasticity or damage onset. Compute the initial elastic stiffness, yield stress, and damage driving force as $Y_{(0)} = \frac{1}{2} E_{(0)} \epsilon^2_{(0)}$.
2. At the first unloading cycle, extrapolate the curve to the abscissa. Compute the stiffness of the first unloading curve $E_{(1)}$ and the remaining plastic strain $\epsilon_{p(1)}$.
3. From the plastic strain compute the corresponding elastic strain $\epsilon_{el(1)}$ and the damage driving force at the first unloading $Y_{(1)} = \frac{1}{2} E_{(0)} \epsilon^2_{el(1)}$. Then compute the damage as $d_{(1)} = 1 - E_{(1)}/E_{(0)}$. Plot the damage and driving force at the first unloading.
4. Compute the (undamaged) effective stress $\tilde{\sigma}_{(1)} = \frac{\sigma_{(1)}}{(1-d_{(1)})}$. From that, compute the isotropic hardening stress $\kappa_{(1)} = \tilde{\sigma}_{(1)} - \sigma_y$ at the first unloading cycle, and plot it against the plastic strain.
5. Repeat steps 2 to 4 at each unloading cycle to track how the damage develops with respect to the driving force as well as how

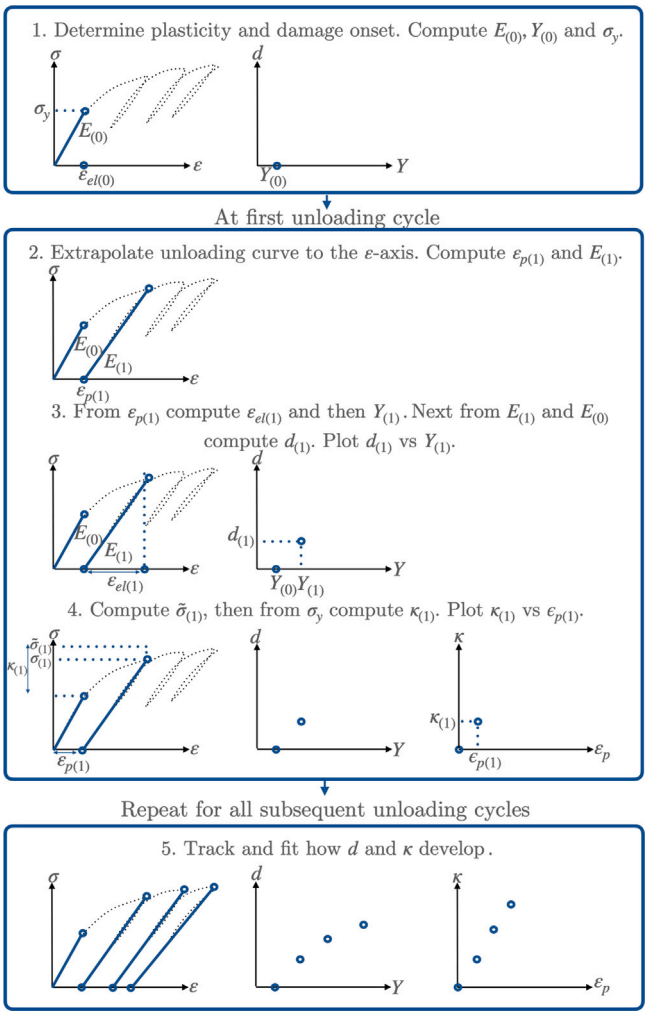

Fig. 4. Illustration of damage and plasticity identification routine.

the isotropic hardening stress develops in terms of the plastic strain.

Once steps 1 through 5 are completed for each uniaxial test (in the reinforcement directions) and in shear, a function and fit for the damage variables as a function of damage driving force can be proposed, i.e. $d_s(Y_s)$ and $d_I(Y_I)$ for $I = 1, 2, 3$. Determining appropriate expressions for $\eta_s(d_s)$ in Eq. (16) and $\eta_I(d_I)$ in Eq. (17), then requires inverting the expressions for the damage such that they are instead given as functions of the damage variables. Finally the expressions for the isotropic hardening stresses $\kappa_s(k_s)$ and $\kappa_I(k_I)$ can be determined by fitting the relationships between the isotropic hardening stresses and their associated plastic strains. This is possible as the flow rules given by Eqs. (25) and (26) imply that for a positive stress, $|\gamma_p| = -k_s$ and $|\epsilon_{p,I}| = -k_I$ for $I = 1, 2, 3$. This procedure for the considered 3D-woven glass fibre reinforced composite material is discussed in more detail in Section 5.2.

4. Implementation

The considered macroscale model for 3D-woven composites was implemented as a user material (UMAT) using the commercial finite element program ABAQUS. Within the finite element framework the evolution of the stress and state variables must be solved locally in the Gauss point. As previously discussed the use of the non-associative yield surfaces in Eqs. (20) and (21), simplifies parameter identification and importantly here, the implementation. In terms of implementation, this makes it possible to decouple the plasticity and damage behaviour and handle them sequentially. For time step ${}^{n+1}t$, this can be done according to the flow chart described in Fig. 5.

Discussing this in more detail, for time step ${}^{n+1}t$:

1. Begin with inserting the strain increment $\Delta\boldsymbol{\epsilon}$ and time increment Δt as well as variables from the previous time step ${}^{n}t$. This include the stress ${}^{n}\boldsymbol{\sigma}$, effective stress ${}^{n}\tilde{\boldsymbol{\sigma}}$, plastic strain ${}^{n}\boldsymbol{\epsilon}_p$, hardening variables ${}^{n}k_s$ and ${}^{n}k_I$, as well as damage variables ${}^{n}d_s$ and ${}^{n}d_I$ for $I = 1, 2, 3$.
2. As the next step, for a given strain increment $\Delta\boldsymbol{\epsilon}$, determine the effective stress $\tilde{\boldsymbol{\sigma}}$ and plastic strain $\boldsymbol{\epsilon}_p$ through the following steps:
   - Compute the effective trial stress, $\tilde{\boldsymbol{\sigma}}_{tr} = {}^{n}\tilde{\boldsymbol{\sigma}} + \mathbb{E} : \Delta\boldsymbol{\epsilon}$. The shear components of the effective trial stress can be computed as $\tilde{\mathbf{s}}_{tr} = \mathbb{Q} : \tilde{\boldsymbol{\sigma}}_{tr}$ where $\mathbb{Q}$ is given by Eq. (11). Similarly the scalar measure of the effective trial tress components along each reinforcement directions can be found as $\tilde{T}^I_{tr} = \tilde{\boldsymbol{\sigma}}_{tr} : \boldsymbol{A}^I$, for $I = 1, 2, 3$.
   - Check the four yield surfaces given in Eqs. (20) and (21) using the effective trial stress measures. Record which yield surfaces are indicating plastic behaviour. This will determine what is found in the vector $\boldsymbol{I}$ to be introduced in the following step.
   - Initialise the solution vector $\boldsymbol{X}$. The desired converged quantities are

$$\boldsymbol{X} = \begin{bmatrix} \tilde{\mathbf{s}} & \Delta\lambda_s & \tilde{T}^1 & \Delta\lambda_1 & \tilde{T}^2 & \Delta\lambda_2 & \tilde{T}^3 & \Delta\lambda_3 \end{bmatrix}^T.$$

   - Begin iteration scheme. Compute the residual $\boldsymbol{R} = [\boldsymbol{R}_s \quad \boldsymbol{R}_1 \quad \boldsymbol{R}_2 \quad \boldsymbol{R}_3]$ and the Jacobian $\boldsymbol{J} = \partial\boldsymbol{R}/\partial\boldsymbol{X}$. The residual vector is composed by considering the backwards Euler expansion of the effective stress components and the yield surfaces in Eqs. (16) and (17). That is

$$\boldsymbol{R}_s = \begin{bmatrix} \tilde{\mathbf{s}} - {}^{n}\tilde{\mathbf{s}} - \mathbb{Q} : \mathbb{E}_m : \left(\Delta\boldsymbol{\epsilon} - \Delta\lambda_s \frac{\tilde{\mathbf{s}}}{\sqrt{2|\tilde{\mathbf{s}}|}} \right) \\ \phi_{p,s} \end{bmatrix} \tag{35}$$

   and

$$\boldsymbol{R}_I = \begin{bmatrix} \tilde{T}^I - {}^{n}\tilde{T}^I - \mathbb{E}_f : \boldsymbol{A}^I : \left(\Delta\boldsymbol{\epsilon} - \Delta\lambda_I \mathrm{sgn}(\tilde{\boldsymbol{\sigma}} : \boldsymbol{A}^I)\boldsymbol{A}^I \right) \\ \phi_{p,I} \end{bmatrix}$$

   for $I = 1, 2, 3,$ (36)

   where $\mathbb{E}_f = \mathbb{E}_{f,1} + \mathbb{E}_{f,2} + \mathbb{E}_{f,3}$. Note that the yield surfaces require the calculation of $\kappa_s(k_s)$ and $\kappa_I(k_I)$. The hardening variables can be computed as $k_s = {}^{n}k_s - \Delta\lambda_s$ and likewise ${}^{n}k_s = {}^{n}k_I - \Delta\lambda_I$
   - Based on the results of the trial yield surface in the previous steps, determine which rows of $\boldsymbol{R}$ should be considered. For example, if only $\phi_{p,s} > 0$, then the active rows are the first seven, i.e $\boldsymbol{I} = [1:7]$. Update the solution vector $\boldsymbol{X}\{\boldsymbol{I}\}$ using the Newton–Raphson method. Here, the brackets $\{\cdot\}$ indicate which rows/columns should be considered in the calculation.
   - Once convergence is reached (i.e. when the norm of the considered rows of the residual vector is less than the desired tolerance) compute the plastic strain $\boldsymbol{\epsilon}_p$. This is done by considering the Backwards-Euler method and from Eqs. (22) and (23). From the plastic strain, the elastic strain can be determined, i.e. $\boldsymbol{\epsilon}_{el} = \boldsymbol{\epsilon} - \boldsymbol{\epsilon}_p$.
   - From the elastic strain, compute the converged effective stress $\tilde{\boldsymbol{\sigma}}$.
3. Once the elastic strain is known, it is possible to determine the damage state of the material.

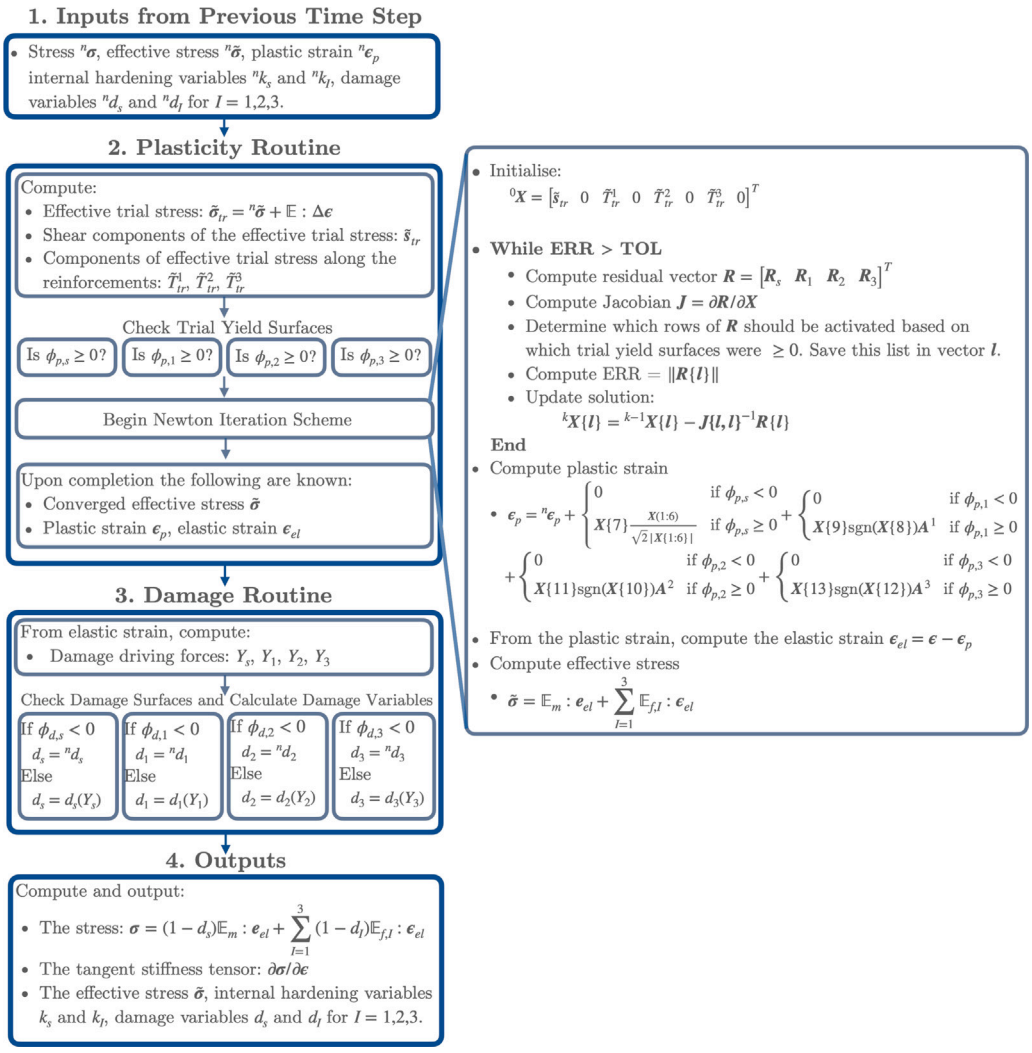

Fig. 5. Implementation of the proposed model.

- Compute the damage driving forces Y_s and Y_I according to Eqs. (18) and (19) respectively.
- Check the damage surfaces $\phi_{d,s}$ and $\phi_{d,I}$ given by Eqs. (16) and (17). Compute the damage variables d_s and d_I, for $I = 1, 2, 3$.

4. In the final section, the stress $\boldsymbol{\sigma}$ can be computed according to Eq. (14) and output along with the tangent stiffness tensor $\partial\boldsymbol{\sigma}/\partial\boldsymbol{\epsilon}$. The updated values for the effective stress $\tilde{\boldsymbol{\sigma}}$, hardening variables k_s and k_I, as well as damage variables d_s and d_I for $I = 1, 2, 3$ must also be output.

5. Results

A testing campaign is currently underway in order to determine the behaviour of a 3D-woven glass fibre reinforced epoxy material. Overall the material's behaviour shows a strong anisotropic response and behaviours which are highly dependent on loading direction. Loading along the warp yarns shows a nearly linear response up until failure. Loading along the horizontal weft yarns however, and in shear, shows a prominent non-linear response. This highlights the need for a flexible modelling framework in which various non-linear phenomena can be added when and where they are needed.

In the following section, the experimental tests will be briefly introduced along with the considered material's elastic properties. The proposed 1D parameter identification routine is then applied and the damage and hardening behaviours are determined for each loading direction. Due to limitations in available test results, only in plane tensile and shear properties will be considered. They will be validated against an in-plane off-axis tensile test. In the event that out-of-plane results are available, a similar method may be used to determine their plasticity and damage parameters.

5.1. Summary of elastic material parameters and experimental testing

The elastic material parameters for the considered glass fibre reinforced epoxy produced by Biteam AB are shown in Table 1. The test specimens were manufactured using resin film infusion with MTFA500 epoxy supplied by SHD Composites. The glass fibres were Hybron 2026 XM (R-glass) 1200 Tex rovings from PPG Fibre Glass. The RVE size is approximately 15 mm in the warp direction, 5 mm in the horizontal weft direction and 1.3 mm in the vertical weft direction. The fibre volume fraction of the material is approximately 0.45. In order to study the displacements and strain fields of all test samples, digital image correlation (DIC) was used.

Tensile testing in the warp and horizontal weft direction were carried out according to the ASTM D3039 standard (ASTM, 2013). A grip distance of 60 mm was used when testing in the warp direction, while a distance of 70 mm was used in the horizontal weft direction. In both cases the tensile test specimens had a width of 25 mm. The

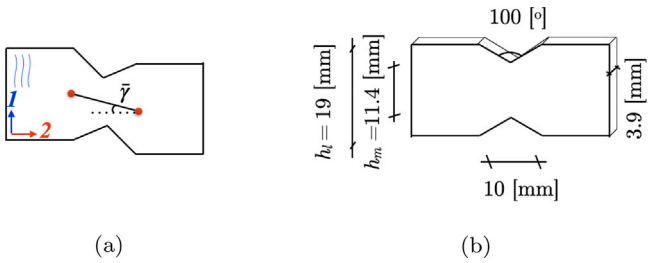

Fig. 6. Illustrations of the Iosipescu shear test.

Table 1
Considered elastic parameters, where $1, 2, 3$ represent the warp, horizontal weft and vertical weft directions respectively. Those marked with an asterisk are assumed values and have not been determined experimentally.

Stiffness	E_{11}	25 [GPa]	E_{22}	13 [GPa]	E_{33}	9 [GPa]
Shear stiffness	G_{12}	1.8 [GPa]	G^*_{13}	1.8 [GPa]	G^*_{23}	1.8 [GPa]
Poisson's ratio	ν_{12}	0.21 [–]	ν^*_{13}	0.30 [–]	ν_{23}	0.3 [–]

in-plane shear behaviour was evaluated using an Iosipescu shear test according to the ASTM D5379 standard with the warp yarns oriented vertically, shown in Fig. 6(a). In this case, due to the variation between E_{11} and E_{22} a notch angle of 100° was chosen following the work of Melin and Neumeister (2006). Again, DIC was used to analyse all test samples. The average shear strain was extracted by tracking the distance between the points indicated in red in Fig. 6(a) and computing the angle between them denoted $\bar{\gamma}$. Assuming linear elasticity and that the resulting shear force in each cross section must be the same, the shear strain in the specimen centre (in the middle between the two notches) can be computed by

$$\gamma = \frac{2\bar{\gamma}}{(1 + h_m/h_l)}. \tag{37}$$

The variables h_m and h_l indicate the height of the gauge region and the height of the total specimen respectively. They are shown in Fig. 6(b) along with the remaining geometric parameters of the test sample.

Although only fully applicable for the linear elastic part of the material behaviour, Eq. (37) was used to estimate the local strain for the whole loading cycle, thus serving as the strain measure in the model calibration described below. The consequences of this simplification is further assessed in Section 5.4

5.2. Calibration and parameter identification from coupon testing

The experimental stress–strain result from cyclic loading along the warp direction is shown in Fig. 7. Following the procedure outlined in Section 3, the associated damage and isotropic hardening stress development at each unloading cycle are plotted. For simplicity, and as for example accelerometer or acoustic emissions data is unavailable, it is assumed that damage and plasticity begin developing at the same location. The initial elastic stiffness is then estimated from the region shown in blue. At each unloading cycle, the stress–strain curve showed a minor increase in stiffness, which manifests itself as a negative damage development when plotted against the damage driving force. It likely indicates that when loaded along the warp reinforcement direction, there is very little progressive damage, but rather a brittle final rupture.

Tracking the development of inelastic strain however, shows that it is necessary to account for plasticity in the warp direction. Here, it is considered sufficient to describe the hardening as linear, i.e. $\kappa_1 = -H_1 k_1$ with hardening modulus H_1. The hardening modulus H_1 as well as the associated yield stress $\sigma_{y,1}$ are summarised in Table 3.

Turning now to the resulting stress–strain curve produced by a cyclic tensile test in the horizontal weft direction, shown in Fig. 8, it is clear that at each unloading cycle there is a progressive loss of stiffness until the damage eventually saturates. In order to fit the damage development behaviour an exponential curve with saturation is considered. The expression for damage development and the calibrated values for the required parameters are again given in Table 2 for the horizontal weft direction. The related damage surface is also given in Table 2.

When it comes to capturing the plastic behaviour of the curve, from Fig. 8, it is again clear that linear hardening is sufficient for describing the isotropic hardening stress vs plastic strain response. The hardening modulus H_2, the yield stress $\sigma_{y,2}$ and the related yield surface are given in Table 3.

Finally, considering the cyclic shear stress–strain response of the in-plane shear specimen (see Fig. 9), it is clear that both the damage and plasticity development are well represented by exponential curves with saturation. Note that in this case, as there are unloading cycles beginning earlier in the test, which show a reduction in stiffness, the onset of damage is assumed to take place before the onset of plasticity. As such the yield stress should be calibrated using the effective stress value at plasticity onset. Again, the damage function, damage surface and parameters are summarised in Table 2. Similarly the yield surface and its associated values found in Table 3

5.3. Uniaxial tensile and pure shear loading behaviour

As a first evaluation of the proposed model, consider the case of loading to produce uniaxial and shear stress states on the material point level. The resulting stress–strain curves for such loading along the warp, horizontal weft and in in-plane shear are shown in Figs. 10(a)–10(c) respectively. Under these ideal load cases, the proposed model and parameter identification scheme is able to effectively capture the experimental material behaviour. It is however necessary to next evaluate the model predictions under more complex loading scenarios.

5.4. Iosipescu FE-model behaviour

In the case of pure shear loading at the material point level, the proposed model is able to accurately capture the stress–strain response. Here however, as the data-reduction (i.e. strain calculation) is associated with simplifying assumptions, the behaviour of an FE-model of the shear Iosipescu test is also evaluated. A three dimensional FE-model of the gauge region was built in ABAQUS using fully integrated linear hexahedral 3DC8 elements. In terms of selecting boundary conditions, it was important to note that the test sample showed some slippage in the grips during the loading and unloading process. In order to account for this the vertical and horizontal displacements were extracted from the DIC image along the boundaries of the gauge region. At each frame the extracted vertical and horizontal displacements were fit linearly as a function of the height of the sample to smooth any noise in the DIC analysis. The displacements were then mapped onto an FE-model of the gauge region and used as boundary conditions in the analysis.

The simulation and experimental results are compared in Fig. 11(a). The force is plotted against the shear angle $\bar{\gamma}$, where again $\bar{\gamma}$ is illustrated in Fig. 6(b). The experimental and simulation results show fair agreement. It can be seen that the initial elastic stiffness is somewhat underestimated by the model, while eventually as the displacement increases the stiffness is somewhat overestimated. This is likely due to the well known challenges associated with achieving pure shear loading when testing composite materials. Fig. 11(b) shows the experimental strain signal γ and the equivalent value extracted from the FE simulation according to Eq. (37). Fig. 11(b) also shows the shear strain value extracted from an integration point in the middle of the gauge region in the FE model. It is clear that the shear strain measure extracted according to that discussed in Section 5.1 is comparable in both the experiment and simulation. The considered strain measure however

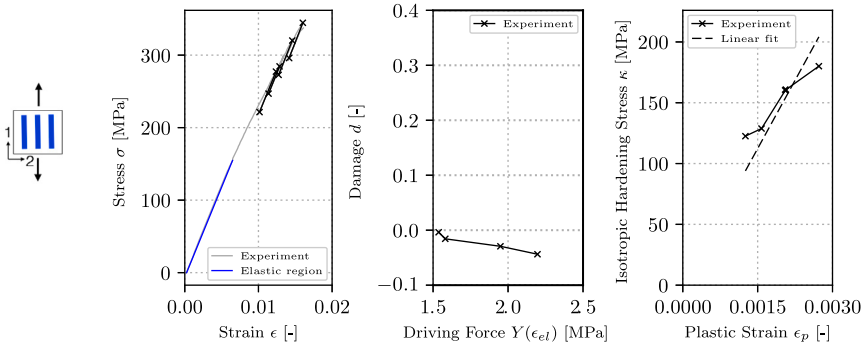

Fig. 7. Parameter identification for damage and plasticity for tensile loading in the warp direction.

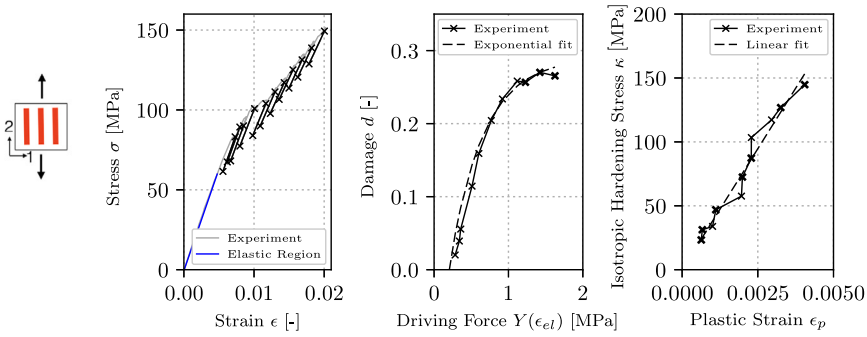

Fig. 8. Parameter identification for damage and plasticity for tensile loading in the horizontal weft direction.

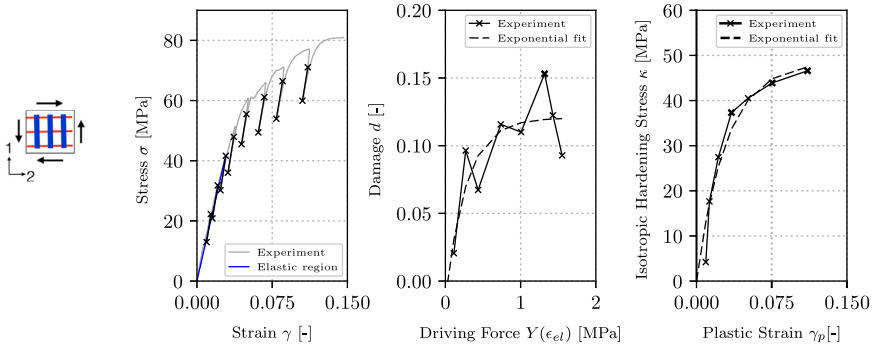

Fig. 9. Parameter identification for damage and plasticity for tensile loading in in-plane shear.

Table 2
The damage parameters.

Direction	Damage variable	Damage onset surface	Parameters
Warp	$d_1 = 0$	–	–
Horizontal weft	$d_2 = d_{sat,2}\left(1 - e^{-b_2(Y_2 - Y_{0,2})}\right)$	$\phi_{d,2} = Y_2 - \left(\frac{-\ln(1-d_2/d_{sat,2})}{b_2} + Y_{0,2}\right)$	$Y_{0,2} = 0.20$ [MPa] $b_2 = 2.20$ [1/MPa] $d_{sat,2} = 0.29$ [–]
Shear	$d_s = d_{sat,s}\left(1 - e^{-b_s(Y_s - Y_{0,s})}\right)$	$\phi_{d,s} = Y_s - \left(\frac{-\ln(1-d_s/d_{sat,s})}{b_s} + Y_{0,s}\right)$	$Y_{0,s} = 0.03$ [MPa] $b_s = 3.63$ [1/MPa] $d_{sat,s} = 0.12$ [–]

does not identically reflect the local shear strain value obtained in the integration point in the middle of the gauge region in the FE model.

Contour plots of the shear strain distributions for the simulations and experiments are shown in Fig. 12. They correspond to a shear angle of $\bar{\gamma} = 0.02$, 0.05 and 0.08 radians respectively. While the overall force-shear angle behaviour of the material can be well captured, an equally exact comparison of the shear strain distributions is challenging. This is because the homogeneous nature of the proposed macroscale model does not allow for the identification and prediction of strain localisation behaviours caused by the heterogeneous mesostructure of the material.

5.5. Off-axis validation

Model validation was carried out by considering an off-axis tensile specimen with the horizontal weft yarns oriented at a ten degree offset to the loading direction. A three-dimensional FE model using 3DC8

Table 3
The plasticity parameters.

Direction	Hardening law	Yield surface	Parameters
Warp	$\kappa_1 = -H_1 k_1$	$\phi_{p,1} = \lvert\tilde{T}^1\rvert - \sigma_{y,1} - \kappa_1$	$H_1 = 81.8$ [GPa] $\sigma_{y,1} = 161$ [MPa]
Horizontal weft	$\kappa_2 = -H_2 k_2$	$\phi_{p,2} = \lvert\tilde{T}^2\rvert - \sigma_{y,2} - \kappa_2$	$H_2 = 37.8$ [GPa] $\sigma_{y,2} = 59.9$ [MPa]
Shear	$\kappa_s = \kappa_{sat,s}\left(1 - e^{c_s k_s}\right)$	$\phi_{p,s} = \frac{1}{\sqrt{2}}\lvert\bar{s}\rvert - \tau_y - \kappa_s$	$\kappa_{sat,s} = 48.6$ [MPa] $\tau_y = 45.4$ [MPa], $c_s = 33.8$ [−]

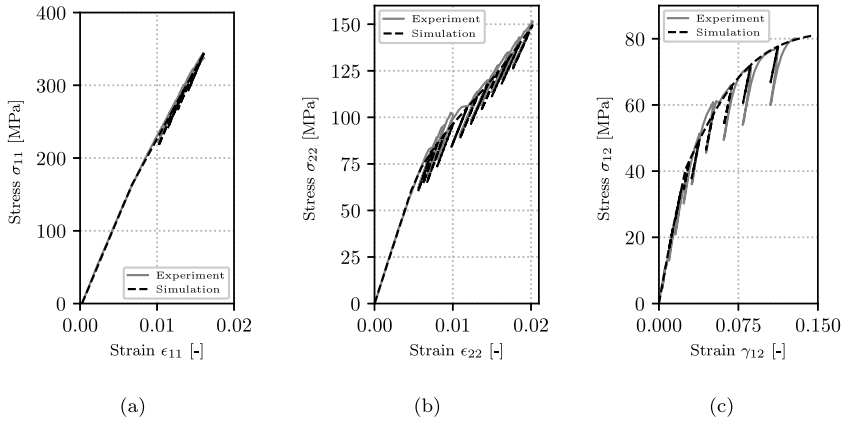

Fig. 10. Stress–strain curves (a) Uniaxial loading in warp direction. (b) Uniaxial loading in horizontal weft direction. (c) Loading in in-plane shear.

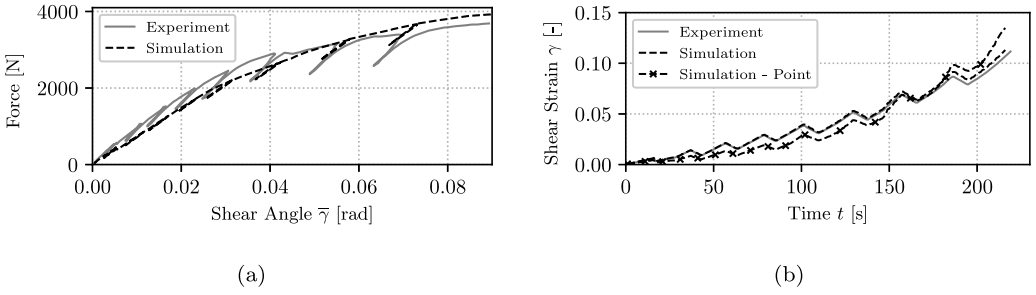

Fig. 11. Comparison of experimental and simulation results for the Iosipescu shear test. (a) Comparison of the force-shear angle curve. (b) Comparison of the strain measures. The shear angle $\bar{\gamma}$ was computed according to Fig. 6(a). The shear strain γ was computed according to Eq. (37). The *Simulation-Point* value was extracted at an integration point in the middle of the gauge region.

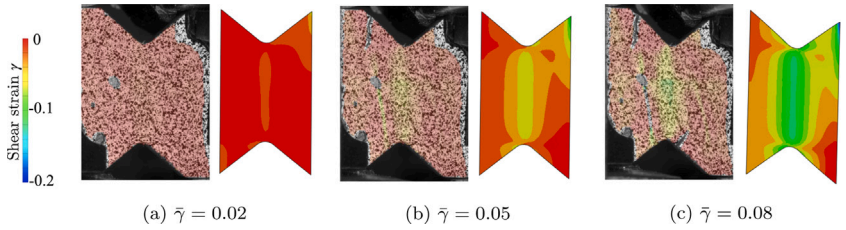

Fig. 12. Comparison of shear strain distributions in the experiment and simulation.

elements was again constructed in ABAQUS with the displacement driven boundary conditions illustrated in Fig. 13(a). The magnitude of the applied boundary displacement was determined based on the DIC data of the corresponding experiment. To obtain a representative measure of the average specimen deformation, a virtual extensometer with an initial separation of 30 mm was placed over the approximate centre of the specimen to extract the axial strain from the DIC data. Based on the length of the specimen, comparable boundary conditions to achieve the same global strain value were applied to the FE model. The size of the test specimen between the grips and the corresponding FE-model are shown in Fig. 13(b).

Fig. 14 compares the resulting force–displacement curves for the experiment and simulation results. Further, the axial strain distribution for both cases is compared in the contour plots in Fig. 15 for varying displacement values. When it comes to the over all force–displacement behaviour, the model is able to accurately predict the experimental test results, in particular in the initial part of the curve. After the third unloading cycle, some variation in the results is apparent. As previously discussed however, the nature of the macroscale model means it is not possible to capture the strain localisations found in the experimental test in between the yarn bundles.

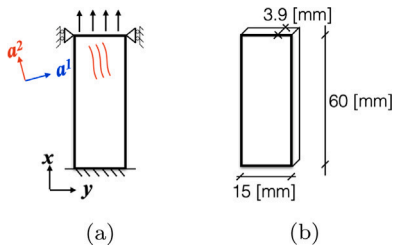

Fig. 13. Illustration of the off-axis tensile specimen.

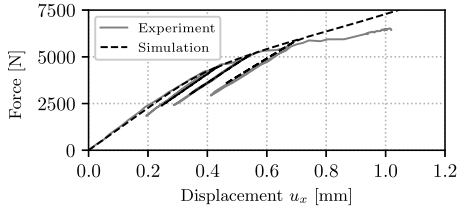

Fig. 14. Force–displacement curves for the off-axis tensile test.

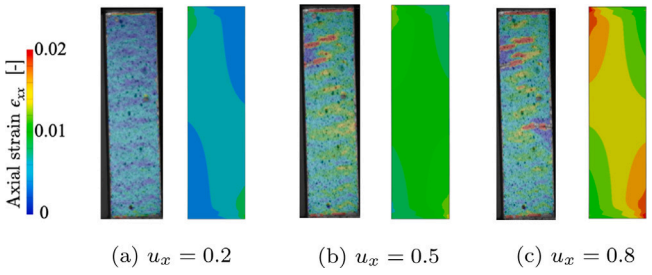

Fig. 15. Comparison of shear strain distributions in the experiment and simulation.

6. Conclusions

Across multiple industries, there is a need for lightweight materials that show high in and out-of-plane strength and stiffness, fracture toughness, damage tolerance and energy absorption capabilities. Composites with 3D-woven reinforcements show promising characteristics that could fulfil these requirements. However, computationally efficient and industrially applicable models are still required to further drive their use.

With this in mind a macroscale model for 3D-woven composites, which treats the material as a homogeneous orthotropic solid has been proposed in this work. The thermodynamically consistent model subdivides the stress and strain components, and in turn the constitutive relation that relates them, into four different terms: one representing each reinforcement direction and one in shear. This decomposition allows for the introduction of four scalar damage variables and separate inelastic material behaviour in a modular fashion depending on loading direction. The separation of the damage and yield surfaces by reinforcement directions and shear creates a model that can be calibrated and implemented in a relatively straightforward manner.

The predictive capability of the model was demonstrated by considering a 3D-woven glass fibre reinforced epoxy. The development of damage and plastic strain was characterised by considering tensile testing with unloading cycles in the warp and horizontal weft directions as well as in in-plane shear. Good agreement between experimental and simulation results was achieved when the model was validated against an off-axis tensile test.

As a conclusion, the current proposed model is considered to be sufficiently detailed to capture the observed behaviours in the experimental results that are available. However, damage and permanent strain growth under multiaxial loading scenarios, compressive loading, loss of orthotropy, or possible couplings between normal and shear behaviours are aspects which have yet to be well understood.

Inducing such loading scenarios and assessing the coupling of the damage and plastic behaviours on experimental test specimens is not trivial. One promising path to addressing these concerns however is using mesoscale models of the 3D-woven composite to simulate different load combinations and produce virtual calibration data. This topic will be further explored and addressed in future work.

Declaration of competing interest

The authors declare that they have no known competing financial interests or personal relationships that could have appeared to influence the work reported in this paper.

Acknowledgements

The project is financially supported mainly by the Swedish Energy Agency under contract 2016-008713. M. Fagerström also gratefully acknowledges the financial support through Vinnova's strategic innovation programme LIGHTer (LIGHTer Academy grant no. 2020-04526). The simulations were performed on resources at Chalmers Centre for Computational Science and Engineering (C3SE) provided by the Swedish National Infrastructure for Computing (SNIC).

Appendix

The initial assumption for the calibration scheme described in Section 5.2 is that in one dimension the stress–strain constitutive relationship of the shown curves can be described by

$$\sigma = (1 - d) E \, \epsilon_{el}. \tag{38}$$

In the case of the full 3D formulation, assuming that the nominal reinforcement directions align with the main coordinate axis, the damaged stiffness tensor in Eq. (14) in Voigt form simplifies to Eq. (39) (given in Box I).

In order to evaluate how the 3D constitutive stress–strain relationship reduces under a uniaxial stress state, the case of tensile loading in the horizontal weft direction can be considered. As such $d_1 = d_3 = 0$. By taking the expression in Eq. (39), inverting it, and assuming a uniaxial stress state defined solely by σ_{22}, the following expression is found

$$\sigma_{22} = \left(1 - d_2 + \frac{d_2^2 A}{C}\right) E_2 \, \epsilon_{el,22}. \tag{40}$$

The constants C and A are defined respectively as

$$A = {E_2}^2 {\nu_{12}}^2 + 2 E_2 E_3 \nu_{12} \nu_{23} \nu_{13} + E_1 E_3 {\nu_{23}}^2 \tag{41}$$

$$C = 4 {E_2}^2 {\nu_{12}}^2 - 4 E_1 E_2 + E_2 E_3 \left(4 {\nu_{13}}^2 + 8 \nu_{12} \nu_{23} \nu_{13}\right) + 4 E_1 E_3 {\nu_{23}}^2. \tag{42}$$

Comparing Eqs. (38) and (40), it is seen that the main difference lies in the extra term containing the squared damage variable.

If we now consider, as an example, the material parameters given by Table 1, the constants A and C can be determined. In turn, the expression given by Eq. (40) becomes

$$\sigma_{22} = (1 - d_2 - 0.061 \, d_2^2) E_2 \, \epsilon_{el,22}. \tag{43}$$

As the damage variable associated with the horizontal weft direction saturates at a value of $d_2 = 0.29$, this additional term amounts to at most an error in the reduced stiffness of 0.5%. For this reason, in order to simplify the calibration routine described in Section 5.2, the one dimensional relationship given by Eq. (38) has been assumed. It should

$$\underline{\mathbb{E}} = \begin{bmatrix} \frac{(1-d_1)E_1(1-\nu_{32}\nu_{23})}{\Delta} & \frac{(1-d_1)(1-d_2)E_1(\nu_{21}+\nu_{31}\nu_{23})}{\Delta} & \frac{(1-d_1)(1-d_3)E_1(\nu_{31}+\nu_{21}\nu_{32})}{\Delta} & 0 & 0 & 0 \\ \frac{(1-d_1)(1-d_2)E_2(\nu_{12}+\nu_{13}\nu_{32})}{\Delta} & \frac{(1-d_2)E_2(1-\nu_{31}\nu_{13})}{\Delta} & \frac{(1-d_2)(1-d_3)E_2(\nu_{32}+\nu_{31}\nu_{12})}{\Delta} & 0 & 0 & 0 \\ \frac{(1-d_1)(1-d_3)E_3(\nu_{13}+\nu_{12}\nu_{23})}{\Delta} & \frac{(1-d_2)(1-d_3)E_3(\nu_{23}+\nu_{13}\nu_{21})}{\Delta} & \frac{(1-d_3)E_3(1-\nu_{12}\nu_{21})}{\Delta} & 0 & 0 & 0 \\ 0 & 0 & 0 & (1-d_s)G_{12} & 0 & 0 \\ 0 & 0 & 0 & 0 & (1-d_s)G_{23} & 0 \\ 0 & 0 & 0 & 0 & 0 & (1-d_s)G_{13} \end{bmatrix} \tag{39}$$

Box I.

be emphasised, however, that Eq. (40) can always be used for a more detailed, although a bit more cumbersome, parameter identification.

References

ASTM, 2013. D3039/D3039M - Standard Test Method for Tensile Properties of Polymer Matrix Composite Materials. ASTM.

Bogdanovich, A.E., 2007. Advancements in manufacturing and applications of 3-D woven preforms and composites. In: ICCM International Conferences on Composite Materials.

De Luycker, E., Morestin, F., Boisse, P., Marsal, D., 2009. Simulation of 3D interlock composite preforming. Compos. Struct. 88, 615–623.

El Said, B., Daghia, F., Ivanov, D., Hallett, S.R., 2018. An iterative multiscale modelling approach for nonlinear analysis of 3D composites. Int. J. Solids Struct. 132–133, 42–58.

Green, S.D., Matveev, M.Y., Long, A.C., Ivanov, D., Hallett, S.R., 2014. Mechanical modelling of 3D woven composites considering realistic unit cell geometry. Compos. Struct. 118, 284–293.

Hirsekorn, M., Marcin, L., Godon, T., 2018. Multi-scale modeling of the viscoelastic behavior of 3D woven composites. Composites A 112, 539–548.

Hurmane, A., Mavel, A., Paulmier, P., Laurin, F., 2016. Combined experimental and modelling approaches for strength analysis of 3D woven composites: from elementary coupons to complex aeronautical structures. AerospaceLab J. 1–11.

Kazemahvazi, S., Khokar, N., Hallstrom, S., Wadley, H.N., Deshpande, V.S., 2016. Confluent 3D-assembly of fibrous structures. Compos. Sci. Technol. 127, 95–105.

Khokar, N., Winberg, F., Hallström, S., 2015. Novel 3D preform architecture for performance and reliability of structural beams. In: ICCM International Conferences on Composite Materials. pp. 19–24.

Ladeveze, P., LeDantec, E., 1992. Damage modelling of the elementary ply for laminated composites. Compos. Sci. Technol. 43 (3), 257–267.

Lemaitre, J., 1992. A Course on Damage Mechanics. Springer-Verlag.

Lomov, S.V., Bogdanovich, A.E., Ivanov, D.S., Hamada, K., Kurashiki, T., Zako, M., Karahan, M., Verpoest, I., 2009. Finite element modelling of progressive damage in non-crimp 3D orthogonal weave and plain weave E-glass composites. In: 2nd World Conference on 3D Fabrics. pp. 1–12.

Lomov, S.V., Ivanov, D.S., Verpoest, I., Zako, M., Kurashiki, T., Nakai, H., Hirosawa, S., 2007. Meso-FE modelling of textile composites: Road map, data flow and algorithms. Compos. Sci. Technol. 67, 1870–1891.

Marcin, L., 2010. Modélisation du Comportement, de L'endommagement et de la Rupture de Matériaux Composites à Renforts Tissés Pour le Dimensionnement Robuste de Structures (Ph.D. thesis).

Melin, L.N., Neumeister, J.M., 2006. Measuring constitutive shear behavior of orthotropic composites and evaluation of the modified Iosipescu test. Compos. Struct. 76, 106–115.

Nathan, S., 2015. Positive reinforcement: 21st century 3D weaving.

Oddy, C., Ekh, M., Ekermann, T., Hallström, S., Fagerström, M., 2021. A framework for macroscale modelling of inelastic deformations in 3D-woven composites. Mech. Mater. 160 (March).

Spencer, A., 1984. Continuum Theory of the Mechanics of Fibre-Reinforced Composites. Springer-Verlag.

Stig, F., Hallström, S., 2012a. A modelling framework for composites containing 3D reinforcement. Compos. Struct. 94, 2895–2901.

Stig, F., Hallström, S., 2012b. Spatial modelling of 3D-woven textiles. Compos. Struct. 94, 1495–1502.

Zscheyge, M., Böhm, R., Hornig, A., Gerritzen, J., Gude, M., 2020. Rate dependent non-linear mechanical behaviour of continuous fibre-reinforced thermoplastic composites – Experimental characterisation and viscoelastic-plastic damage modelling. Mater. Des. 193, 108827.